Statistical approach for electrochemical evaluation of the effect of heat treatments on the corrosion resistance of AlSi10Mg alloy by laser powder bed fusion

M. Cabrini[a,b,c,*], *S. Lorenzi*[a,b,c], *C. Testa*[a,b,c], *T. Pastore*[a,b,c], *D. Manfredi*[d], *M. Lorusso*[d], *F. Calignano*[e], *P. Fino*[d,f]

[a]*University of Bergamo – Department of Engineering and Applied Sciences (DISA), Viale Marconi, 5, 24044 Dalmine (BG), Italy, marina.cabrini@unibg.it, sergio.lorenzi@unibg.it, cristian.testa@unibg.it, tommaso.pastore@unibg.it*

[b]*Consorzio Interuniversitario per la Scienza e Tecnologia dei Materiali (INSTM) – Unit of Research of Bergamo, Viale Marconi, 5, 24044 Dalmine (BG), Italy*

[c]*Consorzio Interunivarsitario per lo Sviluppo di Sistemi a Grande Interfase (CSGI) – Unit of Research of Bergamo Viale Marconi, 5, 24044 Dalmine (BG), Italy*

[d]*Center for Sustainable Future Technologies CSFT@PoliTo, Istituto Italiano di Tecnologia, Via Livorno 60, 10144 Torino, Italy, diego.manfredi@iit.it , massimo.lorusso@iit.it*

[e] *Dipartimento di Ingegneria Gestionale e della Produzione (DIGEP), Politecnico di Torino, Corso Duca degli Abruzzi 24, 10129 Torino, Italy, flaviana.calignano@polito.it*

[f]*Dipartimento Scienza Applicata e Tecnologia (DISAT), Politecnico di Torino, Corso Duca degli Abruzzi 24, 10129 Torino, Italy, paolo.fino@polito.it*

**presenting author*

Abstract

Laser powder bed fusion (LPBF) is one of the most widespread additive manufacturing (AM) technologies for metals, in which the components are built additively layer upon layer along the *z-axis* (the building direction) perpendicular to the building platform (*xy-plane*). Here, we evaluated the effect of post-processing heat treatments at 200, 300, and 400 °C on the corrosion resistance of AlSi10Mg alloy manufactured by LPBF for two orientations in the building chamber (XY – parallel to the building plane or XZ – perpendicular to the building plane). Electrochemical impedance spectroscopy (EIS) and potentiodynamic polarization tests were conducted at the constant chloride ion concentration of 0.02 M and 23 °C for the as-built and heat-treated specimens. All specimens were polished on the surface and displayed similar behaviors in the EIS tests. The pitting potential results were widely scattered and therefore analyzed using a statistical approach. Statistical data analysis based on analysis of variance technique (ANOVA) was performed. The results confirmed that the population significantly differs only by considering the heat treatments and the building direction plays only minor role. The cumulative distribution curves of pitting potentials showed a decrease in pitting resistance as the temperature of heat treatment increases.

Keywords:, laser powder bed fusion, AlSi10Mg, corrosion, pitting, heat treatment, statistical approach, additive manufacturing.

1. Introduction

Additive manufacturing (AM) is a new family of technologies to create customized and sophisticated objects with advanced attributes (new materials and shapes) while saving time and costs with less scrap production [1]. Thanks to the improved product quality, AM is currently used in the aerospace, automotive, and biomedical industries [2] and others. Among the AM-based approaches, laser powder bed fusion (LPBF) allows the fabrication of near-net shape parts directly from CAD design data, by melting a metallic powder bed with a laser source layer over layer. Alloys that are highly corrosion-resistant, expensive, and hard to work with, such as Co-Cr, Ti-, and Ni-alloys are most often used in the LPBF technology [3]. Aluminum alloys can also be processed with LPBF, even if the actual portfolio is restricted to the Al-Si casting system and to some specific composition [4]. In any case, it could be stated that higher mechanical properties can be achieved for such Al alloys compared to the traditional die-casting procedure, in particular for AlSi10Mg alloy [5]. This alloy, also known as A360, is commonly used for applications as cover plates, instrument cases, and also when a certain corrosion resistance is required, such as for irrigation system parts and outboard motor parts.

On the other side, the LPBF and powder-based AM techniques in general leave the specimens with a rough surface [6], that can decrease the fatigue [7] and cavitation/erosion [8] performances, as demonstrated in previous studies on AlSi10Mg alloy. The superficial conditions modify the corrosion behavior. In [9] some tests were carried out after a post process heat treatment performed at 300 °C for two hours to remove the thermal residual stresses typical of LPBF. It was found that as-built surfaces are vulnerable to corrosion with their lower pitting potentials and higher current density than the same surfaces after a finishing post process, like shot peening or manual polishing.

This was attributed to the different levels of protection from the passive film formed on the as-built surfaces compared to the polished ones [10]. Leon et al. [11] reported that compared to the cast alloy, AlSi10Mg obtained by means of LPBF and heat-treated for stress relief at 300 °C showed a slight improvement in the generalized corrosion resistance in NaCl solution. In that case, the specimens were machined from a block of printed alloy: therefore, the surface are not rough, and have an oxide passive layer formed in air. Similar results were obtained on polished specimens of AM2024 alloy produced by means of LPBF, being helped by the absence of S-phase as well as by the micrometer-sized constituent particles in comparison with the wrought AA2024-T3 [12]. The polished specimens of AlSi10Mg also showed improved fatigue limits, as expected [13]. The corrosion fatigue resistance of polished LPBF specimens is similar [13] or better [11, 14] than the cast alloy, the cavitation erosion behavior was also improved [8].

In the LPBF process, the components are built additively layer upon layer along the building direction, perpendicular to a building platform. It was demonstrated that with AlSi10Mg alloy the orientation relative to the building direction does not influence the tensile resistance of the alloy, while it can affect the ductility (or elongation to rupture) and corrosion resistance. In fact, in a previous study on AlSi10Mg [9], we demonstrated that the exposed face built parallel to the platform showed higher pitting potentials in Harrison's solution than the faces built along the building direction. However, this difference decreases when the surface becomes rougher. For example, the average pitting potential differs by more than 400 mV between the two building orientations for the polished specimens, by about 50 mV for shot-peened specimens, and is almost identical for the as-built surfaces.

Moreover, in terms of microstructure, the AlSi10Mg produced by means of LPBF has a characteristic very fine one due to the extremely rapid interaction between a concentrated laser source and micrometric metallic powders, generating a very fast melting and subsequent solidification rate [3]. This microstructure obviously influences the corrosion morphology of the

alloy. And as expected, both the microstructure and corrosion morphology are modified by post-processing heat treatments. When tested in Harrison's solution at the free corrosion potential, the alloy after LPBF and after the stress relieving treatment described before, showed intense attack at the edge of the melt pool [9]. This selective corrosion was also observed by Revilla et al. in a 0.1 M NaCl solution on the alloy without heat treatment, although those authors found no differences between the building directions [15]. Potentiodynamic tests carried out in Harrison's solution showed similar pitting potentials for polished specimens with or without the stress relieving treatment. On the contrary, annealing treatment at 550 °C significantly lowers the pitting potential [16]. Specimens with the as-built surface could not be evaluated this way, because in these cases pitting was always initiated during the equilibration time and became fully active during the potentiodynamic tests.

The effect of low-temperature heat treatments on the corrosion morphology of the alloy was studied in a previous work [17] by means of selective corrosion tests in a solution 0.51 M of NaCl and 0.12 M of HCl at room temperature for 24 h, according to ISO11846 standard. The susceptibility of alloys to selective corrosion attack was noticed after stress relief by heating to 200–300 °C. The attack became the most intense for the specimen heat-treated at 300 °C. Treatment at higher temperatures (400 °C and 500 °C) produced a marked decrease in hardness but prevented the insurgence of selective corrosion attack. A previous work [18] tried to evaluate the effect of post-processing heat treatment on the pitting potentials in neutral NaCl solutions of different concentrations using the approach of McCafferty [19]. In that case, an approximately logarithmic correlation was observed between the pitting potentials and the activity of the chloride ions, but unfortunately the experimental pitting potentials showed very high variability.

The stochastic nature of pitting initiation requires a statistical approach [20], it was done for stainless steels [21, 22], copper [23], nickel [24] and aluminum alloys [25, 26], but, on the author knowledge, it was never studied on additive manufactured alloys.

In the present paper, the effect of low-temperature heat treatments on the pitting potentials of LPBF AlSi10Mg was evaluated at the constant chloride concentration of 0.02 M, using a statistical approach to limit the dispersion of the data. The cumulative frequency distribution for a large number of specimens was obtained for different building orientations and microstructures. Note that in this work, all the tests were conducted on polished specimens.

2. Experimental

2.1 Materials and specimens

The specimens were prepared using gas-atomized AlSi10Mg alloy powder supplied by EOS GmbH (Electro-Optical Systems, Germany) with the nominal chemical composition shown in Table 1. The detailed description of the specimen manufacturing by LPBF is given in previous works [27, 28]. Disk specimens 15 mm in diameter and 5 mm in height were built with the circular surface perpendicular and parallel to the building platform, which are called XZ and XY specimens, respectively. The as-built specimens without any further heat treatment are named UT, while other built specimens were heat-treated at 200, 300, or 400 °C for 2 h and then cooled in air.

To avoid the effect of a rough surface, all specimens were grinded with abrasive paper to 4000 grit and polished with 0.3 μm colloidal alumina. After the polishing, they were passivated in air for 48 h before testing. Moreover, all specimens were degreased in acetone before the electrochemical tests.

2.2 Electrochemical tests

Electrochemical tests were performed using an Ivium CompactStat instrument with a 1-L ASTM G5-82 glass cell. The cell was equipped with a saturated calomel reference electrode (SCE) placed in a Huber-Luggin capillary probe, and two graphite counter electrodes. The specimens were

inserted into a PTFE sample holder with an exposed surface of 0.785 cm^2 and used as the working electrode. Before the tests, the specimens were immersed in the solution and stabilized for 600 s at the free corrosion potential (E_{cor}). After this equilibration time, the electrochemical impedance spectrum (EIS) was registered using a sinusoidal signal with ±10 mV vs E_{cor} of amplitude in the frequency range between 40000 and 0.01 Hz, with 5 frequency for decade. Each test took about 30 minutes.

Afterwards, the specimens were left in open circuit conditions for 300 s. Then, the potentiodynamic test was conducted with a potential scan rate of 0.167 mV/s, from -10 mV vs E_{cor} to +800 mV vs SCE or up to an anodic current of 1 mA. The range of potentials was chosen in order to have not high cathodic polarization, it is well known that alkalinisation promoted by the cathodic reaction can alter the passive film of aluminum. The final potential was fixed at +800 mV vs SCE but when localized attack occurred at potential lower than + 800 mV vs SCE, the tests were stopped once anodic current reached the value of 1 mA/cm^2. This value was chosen based on authors experience".

The potential at the beginning of rapid current increase was assumed to be the pitting potential. Eight specimens were tested for each condition. The test solution was chosen on the basis of precedent work [18]; in this paper, the effect of the heat treatment temperature on pitting potential was studied at different chlorides concentration. The sodium sulfate was added as supporting electrolyte in order to maintain constant the ohmic resistance of the solution. The obtained results pointed out a high dispersion of the pitting potential, for this reason it was decided to use a statistical approach, increasing the number of specimens for each test condition, but using only one chloride concentration. The chloride concentration that present the higher dispersion of pitting potential was considered. The tests were carried out at 23 °C in an aerated 0.02 M NaCl solution added with 0.29 M Na_2SO_4 as a supporting electrolyte, so as to maintain the Na^+ ion concentration

at about 0.6 M (i.e., the average concentration of sodium chloride in sea water) considering that sodium sulfate does not significantly alter the corrosion behavior of aluminum [29].

After the tests, the specimens were firstly washed with distilled water, rinsed with acetone in ultrasonic bath, and finally dried. Corrosion morphologies were observed by means of optical and scanning electron microscopes.

3. Results and discussion

3.1 Electrochemical behavior

For all the specimens, the averaged open circuit potential (OCP) during the last 100 s of equilibration fall in a range of 300 mV between -0.8 to -0.5 V vs SCE, regardless of the heat treatment and building direction (Fig.1).

The EIS spectra are similar for all the specimens immediately after dipping into the solution, as can be seen in Fig. 2. The low-frequency impedance modulus is high, and the phase angle is approaching zero degrees, thus indicating stable passive conditions. Although it does not correspond to the polarization resistance of the specimen, the difference between the impedance moduli at low and high frequencies can nevertheless allow one to estimate the order of magnitude of the oxide resistance and, so, to the protection conferred by the protective film. Fig. 3 shows these values for different heat treatments. For most specimens, this difference in impedance moduli is between 10^5 to 10^6 Ω cm^2 regardless of the building direction and heat treatment. Such high values indicate the absence of active zones of corrosion. In other words, the just-dipped specimens showed similar values of the impedance modulus regardless of heat treatment and building direction, because the mechanical polishing eliminated any differences in the passive film on the surface, and the oxidation at air formed the same protective film on all the specimens. Polishing, however, does

not remove the poorly protective film formed at high temperature during the manufacturing process that still remains inside emerging porosities. In these zones, relatively high current densities can be hypothesized despite the whole surface around the porosity is still passive. This causes a decrease in the impedance modulus, as shown in Fig. 3. All the EIS spectra presented one time constant, thus indicating passive behavior of the alloy. In fact, once the localized corrosion is triggered, the attack propagates with the dissolution of the aluminum matrix mainly at the edge of the melt pool created by the laser scan track. This selective corrosion process is evidenced in the EIS spectra by the clear separation of the two time constants [9]: one time constant was attributed to the cathodic process on the silicon particles, which are more noble than the aluminum matrix and the passive film on aluminum, while the second time constant is related to the corrosion of the α-Al phase close by [16, 30].

Different potentiodynamic curves were observed on identically prepared specimens, as shown in Fig. 4 for UT-XY. Some curves showed a wide passive range in which no pitting was initiated until the final potential of +0.8 V vs SCE (solid black lines in Fig.4) while other curves presented a reduced range of passivity (black dotted lines in Fig.4). From these curves, it is possible to determine the pitting potential (E_{pit}) as the potential where the anodic current increases. At least, one specimen presented a curve with active corrosion behavior (gray solid line in Fig.4) indicating that pitting was initiated at the corrosion potential during the equilibration time. Similar behaviors were observed in the heat-treated samples.

The polarization resistance obtained by the potentiodynamic curves is well correlated to the impedance modulus at low frequency, but unrelated to E_{cor} or E_{pit}, thus confirming the stochastic nature of the localized corrosion initiation. A table is provided in Supplementary data to summarize the additional E_{cor} and E_{pit}, the impedance modulus, and the polarization resistance data.

Statistical data analysis based on analysis of variance technique (ANOVA) was performed. Data were grouped to carry out a two-way analysis with repeated measures, being the building direction and heat treatment the two parameters and the number of repetitions equal to 8 for each condition. The test was chosen to assess whether the populations could be considered as part of the same population (null hypothesis) or they have to be maintained separated (alternative hypothesis) from each other with a confidence level (LOC) of 95%, which equates to declaring statistical significance at the p-value lower than 5%.

The analysis of main effects showed that the population significantly differs only by considering the heat treatments with very low p-value, of about 0.8%. On the contrary, the building direction plays only minor role as the p-value is high, being 33%. Hence, data were grouped neglecting the different building directions and they have been analyzed based on 16 specimens each heat treatment. No significant interaction between the effects of heat treatment and the building direction on the pitting potential of the alloy was found as the p-value is equal to 7,4%.

A clear negative trend with the heat treatment can be underlined by the cumulative frequency curves of the specimens with different heat-treatment (Fig. 5). The pitting potentials UT specimens are between -0.5 and +0.8 V vs SCE, while the pitting potentials of all other specimens are relatively shifted towards more negative potentials. The specimens heat-treated at 300 °C and 400 °C have similar OCP ranges, between -0.7 V vs SCE and +0.5 V vs SCE. However, the distribution of the specimens treated at 400 °C is more shifted to the right compared to 300 °C, and the average values of the pitting potentials are one hundred millivolt lower than the specimens heat treated at 300°C (-0.313±0.4 for the specimens heat treated at 400 °C and -0.207±0.4 for the specimens heat treated at 300 °C). The alloy exhibits localized corrosion as the temperature of the heat treatment increases. More complex seems to be the behavior of the specimens heat treated at 200°C, that present a very enlarged cumulative frequency distribution. The effect of the heat treatment on the

corrosion behavior can be explained by means of the evolution of the microstructure with temperature.

3.2 Pitting behavior and microstructure

In aluminum alloys, pitting occurs mainly at the interface between the α-Al matrix and the secondary phases [31-32]. In the AlSi10Mg LPBF alloy, the silicon particles are very finely distributed throughout, and their shape and size depend on the printing process and the post-processing heat treatment. Materials produced by LPBF have unique microstructure made by consecutive laser scans tracks (Fig.6 (a)). The microstructure of the alloys, as described in detail by several authors [33-37], depends on the scan strategy, the powder, and the machine used. It generally consists of overlapped tracks of fusion, called the melt pools (MP) as visible in cross sections. Inside the MP, the alloy is constituted by micro-dendrites of α-Al oversaturated with silicon. The undissolved silicon crystalizes on the edge of the micro-dendrites of both separate particles and eutectic phase. Between two overlapping MPs, there is a zone (edge of the melt pool) in which the alloy is melted twice, and another adjacent zone in which the alloy is not melt but heated by the overlying molten metal. This zone is called the heat-affected zone (HAZ, like that in a weld) and has a different microstructure (Fig.7 (a)). In particular, the silicon particles are separated by the aluminum matrix as idiomorphic crystals. The localized corrosion attack is always initiated at the edge of the MP (Fig.8 (a) and (b)). Similar results were obtained in Harrison's solution [9, 16], in 0.6 M NaCl solution [15], and in 0.51M NaCl and 0.12M HCl solution (ISO 11846) at room temperature [17].

The post-processing heat treatments modify the microstructure of the alloys as shown in Fig.6 (b), (c), and (d). For heat treatments below 400 °C, the macrostructure of overlapped MP is maintained, but the silicon particles coalesce to form a continuous network around the α-Al dendrites, the eutectic phase disappears, and on the edge of the MPs idiomorphic crystals of silicon increase in

size (Fig.7 (b) and (c)). The practical nobility of the aluminum matrix depends on the nobler element dissolved, mainly its silicon content. When the silicon is rejected from the oversaturated aluminum matrix to form growing idiomorphic crystal, the matrix becomes less noble. In this way, there is more galvanic stimulation of the aluminum matrix corrosion by means of the silicon particle formation, and the resistance to the trigger of pitting is decreased. The scanning Kelvin probe force microscope (SKPFM) results reported by Revilla et al. [15] on untreated samples evidenced larger differences between the silicon and aluminum phases in the edge of the MP than in the center, and both are less prominent than in the case of cast alloy. A larger difference in the Volta potentials between the two phases in the alloy means increased galvanic corrosion stimulation [38].

On the other hand, the internal stress can also contribute to the initiation of localized corrosion [39-41]. The internal stresses in the XZ direction are higher than that in the XY direction, mainly in the zone where two or more tacks overlap [37]. In addition, Louvis et al. [33] reported the possibility to have in this zone a wall constituted of two thin oxide films separated by a gap in which there is un-melted powder, where the pores are preferentially formed. The discontinuity in the passive film at the crossing of two MPs is also a preferred zone of corrosion attacks, as shown in Fig. 8.

The internal strains decrease with the increasing of the temperature of heat treatment, while on the contrary, the difference of nobility between aluminum and silicon phase increases with it. The oxide at the crossing of two MPs in not influenced by the heat treatment.

The obtained results suggest that, on the UT specimens the increased practical nobility of the silicon-oversaturated aluminum prevails on the residual internal strains. The heat treatment at 300 °C fully removes the residual internal strains, but it also simultaneously depletes the silicon content inside the aluminum matrix. In this way, the effect of galvanic stimulation is emphasized, and as a consequence the pitting resistance decreases.

Perhaps, the heat treatment at 200 °C does not remove the residual internal stresses, and at the same time it could not provoke a significative growth of the silicon particle size. DSC analysis performed by Marola et al. [42] indicated that the silicon diffusion process begins at around 200 °C. Those results would seem to indicate that for some specimens, the higher nobility of the aluminum matrix over-saturated in silicon prevails, and so they showed a corrosion behavior similar to the untreated ones. On the contrary, the effect of residual internal stresses and the oxide at the crossing of two or more MPs seems to prevail in some other specimens, leading to a marked deterioration of corrosion resistance. This could be the reason of the very large distribution in the pitting potentials of these specimens. This aspect will be better explored in future works.

Increasing the temperature of the post-processing heat treatment decreases the hardness and the mechanical properties of the alloy [36, 43]. For heat treatments at higher than 400 °C, the MP microstructure is destroyed, and the silicon separates as rounded particles (Fig. 6 (d) and Fig. 7 (d)). In these conditions the galvanic stimulation of the corrosion is more efficient than for the untreated specimens and those treated at 300 °C. Hence, the pitting initiation is significantly enhanced. A previous work [16] underlined the poor corrosion resistance of the microstructures of coarse rounded particles of silicon in a matrix of aluminum obtained after an annealing treatment at 500 °C: in this case the corrosion attack took place with a generalized morphology.

4. Conclusions

AlSi10Mg alloy samples were produced using LPBF with different building directions, followed by post-processing heat treatment at different temperatures. For the first time, the corrosion behavior of the specimens was examined in 0.02 M NaCl solution at 23 °C by means of EIS and potentiodynamic tests through a statistical approach. The corrosion resistance decreases with increasing temperature of the heat treatment, while the building direction does not seem to influence it. On the basis of these results, the post processing heat treatment are not recommended in the case

in which a high corrosion resistance is required (i.e. in heat exchanger or for aerospace applications). In this last case, a high temperature of the building platform is suggested to avoid the internal residual strain. If the post processing stress relieve treatment must be executed, coating or anodizing treatments should be developed in order to improve the corrosion resistance of the alloy.

Funding

This research did not receive any specific grant from funding agencies in the public, commercial, or not-for-profit sectors.

References

[1] W. Frazier, Metal additive manufacturing: A review, J. Mater. Eng. Perform. 23 (2014) 1917.

[2] N. Guo, M. Leu, Additive manufacturing: Technology, applications and research needs, Front. Mech. Eng. 8 (2013) 215.

[3] D. Herzog, V. Seyda, E. Wycisk, C. Emmelmann, Additive manufacturing of metals, Acta Mater. 117 (2016) 371.

[4] T.B. Sercombe, X. Li, Selective laser melting of aluminium and aluminium metal matrix composites: Review, Mater. Technol., 31 (2016) 77.

[5] N. Read, W. Wang, K. Essa, M. Attallah, Selective laser melting of AlSi10Mg alloy: Process optimization and mechanical properties development, Mater. Design 65 (2015) 417.

[6] T. Mower, M. Long, Mechanical behavior of additive manufactured, powder-bed laser-fused materials, Mater. Sci. Eng. A 651 (2016) 198.

[7] N. Uzan, R. Shneck, O. Yeheskel, N. Frage, Fatigue of AlSi10Mg specimens fabricated by additive manufacturing selective laser melting (AM-SLM), Mater. Sci. Eng. A 704 (2017) 229.

[8] J. Zou, Y. Zhu, M. Pan, T. Xie, X. Chen, H. Yang, A study on cavitation erosion behavior of AlSi10Mg fabricated by selective laser melting (SLM), Wear 376-377, Part A (2017) 496.

[9] M. Cabrini, S. Lorenzi, T. Pastore, S. Pellegrini, D. Manfredi, P. Fino, S. Biamino, C. Badini, Evaluation of corrosion resistance of Al–10Si–Mg alloy obtained by means of Direct Metal Laser Sintering, J. Mater. Process. Technol. 231 (2016), 326.

[10] M. Cabrini, S. Lorenzi, T. Pastore, S. Pellegrini, M. Pavese, P. Fino, E. Ambrosio, F. Calignano, D. Manfredi, Corrosion resistance of direct metal laser sintering AlSiMg alloy, Surf. Interface Anal. 48 (2016) 818.

[11] A. Leon, A. Shirizly, E. Aghion, Corrosion behavior of AlSi10Mg alloy produced by additive manufacturing (AM) vs. its counterpart gravity cast alloy, Metals 6 (2016) 148.

[12] O. Gharbi, D. Jiang, D. Feenstra, S. Kairy, Y. Wu, C. Hutchinson, N. Birbilis, On the corrosion of additively manufactured aluminium alloy AA2024 prepared by selective laser melting, Corros. Sci. 143 (2018) 93.

[13] M. Tang, P. Pistorius, Oxides, porosity and fatigue performance of AlSi10Mg parts produced by selective laser melting, Int. J. Fatigue 94 Part 2 (2017) 192.

[14] N. Aboulkhair, I. Maskery, C. Tuck, I. Ashcroft, N. Everitt, Improving the fatigue behaviour of a selectively laser melted aluminium alloy: Influence of heat treatment and surface quality, Mater. Design 104 (2016) 174.

[15] R. Revilla, J. Liang, S. Godet, I. De Graevea, Local corrosion behavior of additive manufactured AlSiMg alloy assessed by SEM and SKPFM, J. Electrochem. Soc. 164 (2017) C27.

[16] M. Cabrini, S. Lorenzi, T. Pastore, S. Pellegrini, E. Ambrosio, F. Calignano, D. Manfredi, M. Pavese, P. Fino, Effect of heat treatment on corrosion resistance of DMLS AlSi10Mg alloy, Electrochim. Acta 206 (2016) 346.

[17] M. Cabrini, F. Calignano, P. Fino, S. Lorenzi, M. Lorusso, D. Manfredi, C. Testa, T. Pastore, Corrosion behavior of heat-treated AlSi10Mg manufactured by laser powder bed fusion, Materials 11 (2018) 1051.

[18] M. Cabrini, S. Lorenzi, T. Pastore, C. Testa, D. Manfredi, G.Cattano, F. Calignano, Corrosion resistance in chloride solution of the AlSi10Mg alloy obtained by means of LPBF, Surf Interface Anal. (2018) 1-6 https://doi.org/10.1002/sia.6601 in press.

[19] E. McCafferty, The electrode kinetics of pitting initiation on aluminum, Corros. Sci. 37 (1995) 481.

[20] T. Shibata and T. Takeyama, Stochastic Theory of Pitting Corrosion, Corrosion, 33, (1977) 243.

[21] J. Wang, S. Qian, Y. Li, D. Macdonald, Y. Jiang and J. Li, Passivity breakdown on 436 ferritic stainless steel in solutions containing chloride, J. Mat. Sci. & Tech. (2018) https://doi.org/10.1016/j.jmst.2018.10.030.

[22] S. Street, A. Cook, H. Mohammed-Ali, T. Rayment and A. Davenport, The Effect of Deposition Conditions on Atmospheric Pitting Corrosion Location Under Evans Droplets on Type 304L Stainless Steel, 74 (2018) 520.

[23] D. Kong, C. Dong, X. Wei, C. Man, X. Lei, F. Mao and X. Li, Size matching effect between anion vacancies and halide ions in passive film breakdown on copper, Electrochim. Acta 292 (2018) 817.

[24] A. Al-Sahli, E. Ghanbari and D. Macdonald, Effect of tungsten alloying on passivity breakdown of nickel, Mat. and Corros. (2018) 1

[25] S. Pride, J. Scully and J. Hudson, Metastable Pitting of Aluminum and Criteria for the Transition to Stable Pit Growth, J. Electrochem. Soc. 141 (1994) 3028.

[26] P. Aziz , Application of the Statistical Theory of Extreme Values To the Analysis of Maximum Pit Depth Data for Aluminum, Corrosion 12 (1956) 35.

[27] F. Calignano, D. Manfredi, E. Ambrosio, L. Iuliano, P. Fino, Influence of process parameters on surface roughness of aluminum parts produced by DMLS, Int. J. Adv. Manuf. Technol. 67 (2013) 2743.

[28] D. Manfredi, F. Calignano, E. Ambrosio, M. Krishnan, R. Canali, S. Biamino, M. Pavese, E. Atzeni, L. Iuliano, P. Fino, C. Badini, Direct metal laser sintering: an additive manufacturing technology ready to produce lightweight structural parts for robotic applications, Metal. Ital. 105 (2013) 15.

[29] W.C. Moshier, G.D. Davis, J.S. Ahearn, The corrosion and passivity of aluminum exposed to dilute sodium sulfate solutions, Corr. Sci. 27 (1987) 785

[30] R. Buchheit, A compilation of corrosion potentials reported for intermetallic phases in aluminum alloys, J. Electrochem. Soc. 142 (1995) 3994.

[31] P. Fathi, M. Mohammadi, X. Duan, A. Nasiri, A comparative study on corrosion and microstructure of direct metal laser sintered AlSi10Mg_200C and die cast A360.1 aluminum, J. Mater. Process. Technol. 259 (2018) 1.

[32] K. Yasakau, M. Zheludkevich, S. Lamaka, M. Ferreira, Role of intermetallic phases in localized corrosion of AA5083, Electrochim. Acta 52 (2007) 7651.

[33] K. Louvis, L. Fox, C. Sutcliffe, Selective laser melting of aluminium components, J. Mater. Process. Technol. 211 (2011) 275.

[34] L. Thijs, K. Kempen, J.-P. Kruth, J. Van Humbeeck, Fine-structured aluminium products with controllable texture by selective laser melting of pre-alloyed AlSi10Mg powder, Acta Materialia 61 (2013) 1809.

[35] N. Aboulkhair, N. Everitt, I. Ashcroft, C. Tuck, Reducing porosity in AlSi10Mg parts processed by selective laser melting, Addit. Manuf. 1 (2014) 77.

[36] W. Li, S. Li, J. Liu, A. Zhang, Y. Zhou, Q. Wei, C. Yan, Y. Shi, Effect of heat treatment on AlSi10Mg alloy fabricated by selective laser melting: Microstructure evolution, mechanical properties and fracture mechanism, Mater. Sci. Eng. A 663 (2016) 116.

[37] F. Trevisan, F. Calignano, M. Lorusso, J. Pakkanen, A. Aversa, E. Ambrosio, M. Lombardi, P. Fino, D. Manfredi, On the selective laser melting (SLM) of the AlSi10Mg alloy: Process, microstructure, and mechanical properties, Materials 10 (2017) 76, doi: 10.3390/ma10010076.

[38] A. Davoodi, J. Pan, C. Leygraf, S. Norgren, The role of intermetallic particles in localized corrosion of an aluminum alloy studied by SKPFM and integrated AFM/SECM, J. Electrochem. Soc. 155 (2008) C211.

[39] X. Liu, G. Frankel, B. Zoofan, S. Rokhlin, Effect of applied tensile stress on intergranular corrosion of AA2024-T3, Corros. Sci. 46 (2004) 405.

[40] D. Nickel, D. Dietrich, T. Mehner, P. Frint, D. Spieler, T. Lampke, Effect of strain localization on pitting corrosion of an AlMgSi0.5 alloy, Metals 5 (2015) 172.

[41] H. Krawiec, V. Vignal, Z. Szklarz, Local electrochemical studies of the microstructural corrosion of AlCu4Mg1 as-cast aluminium alloy and influence of applied strain, J. Solid State Electrochem. 13 (2009) 1181.

[42] S. Marola, D. Manfredi, G. Fiore, M. Poletti, M. Lombardi, P. Fino, L. Battezzati, A comparison of Selective Laser Melting with bulk rapid solidification of AlSi10Mg alloy, J. Alloy. Compd. 742 (2018) 271.

[43] L. Girelli, M. Tocci, L. Montesano, M. Gelfi, A. Pola, Optimization of heat treatment parameters for additive manufacturing and gravity casting AlSi10Mg alloy, IOP Conf. Series: Materials Science and Engineering 264 (2017) 012016.

[44] D. Dash, S. Kumar, C. Mallika, U. Kamachi Mudali, New data on activity coefficients of potassium, nitrate, and chloride ions in aqueous solutions of KNO3 and KCl by ion selective electrodes, ISRN Chem. Eng. (2012) 730154.

[45] A. Leon, E. Aghion, Effect of surface roughness on corrosion fatigue performance of AlSi10Mg alloy produced by Selective Laser Melting (SLM), Mater. Charact. 131 (2017) 188.

Table Caption

Table 1: Nominal chemical composition of the powder

Figure Captions

Fig. 1. Effect of heat treatment temperature on the OCP in 0.02 M NaCl solution at 23 °C

Fig. 2. Example EIS spectrum of the UT specimen immediately after dipping in 0.02 M NaCl solution at 23 °C; a) XY specimen and b) XZ specimen

Fig. 3. Effect of heat treatment temperature on the difference in electrochemical impedance modulus at 10 mHz and 40 kHz in 0.02 M NaCl solution at 23 °C

Fig. 4. Potentiodynamic curves of the UT-XY specimens in 0.02 M NaCl solution at 23 °C, showing their different behaviors

Fig. 5. Effect of heat treatment temperature on the cumulate frequency of the pitting potentials (16 specimens) (or OCP for the pitting was initiated during the equilibration time) in 0.02 M NaCl solution at 23°C (Black dots: UT; White diamonds: HT200°C; Black triangles: HT300°C; Black squares: HT400°C)

Fig. 6. Microstructure evolution (Keller attack) of AlSi10Mg (XZ plane) using different post-processing treatments: (a) untreated specimen, and specimen heat-treated for 2 h at (b) 200 °C, (c) 300 °C, and (d) 400 °C. The white arrows indicate the building direction (along z-axis)

Fig. 7. High-magnification micrographs at the edge of MP of the AlSi10Mg XZ specimens (a) untreated, (b) after stress relieving treatment at 200°C for 2 hours, (c) after stress relieving treatment at 300°C for 2 hours and (d) after stress relieving treatment at 200°C for 2 hours. The white arrows indicate the building direction (along z-axis)

Fig. 8. Morphology of corrosion after the potentiodynamic tests. (a) UT-XY, (b) UT-XZ, (c) HT@200°C-XY, (d) HT@200°C-XZ, (e) HT@300°C-XY, (f) HT@300°C-XZ, (g) HT@400°C-XY, and (h) HT@400°C-XZ

Table 1: Nominal chemical composition of the powder.

Element	Si	**Fe**	**Cu**	**Mn**	**Mg**	**Ni**	**Zn**	**Ti**	**Al**
% weight	9-11	≤0.55	≤0.05	≤0.45	0.2-0.45	≤0.05	≤0.1	≤0.15	bulk

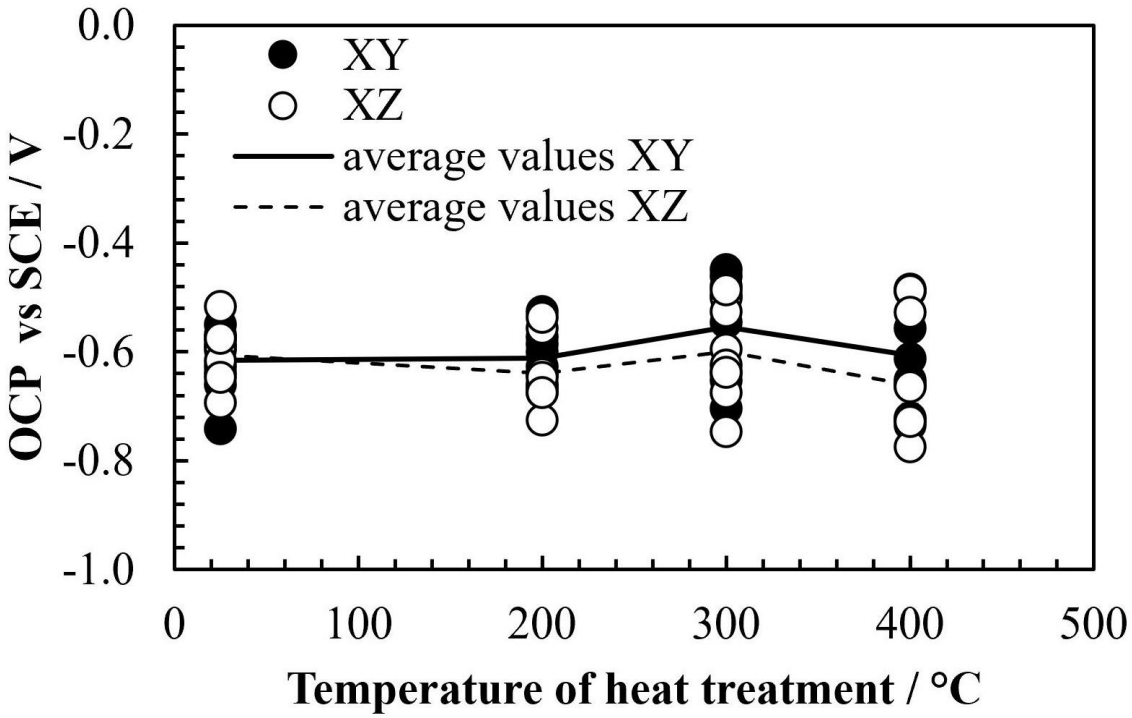

Fig.1. Effect of heat treatment temperature on the OCP in 0.02 M NaCl solution at 23 °C

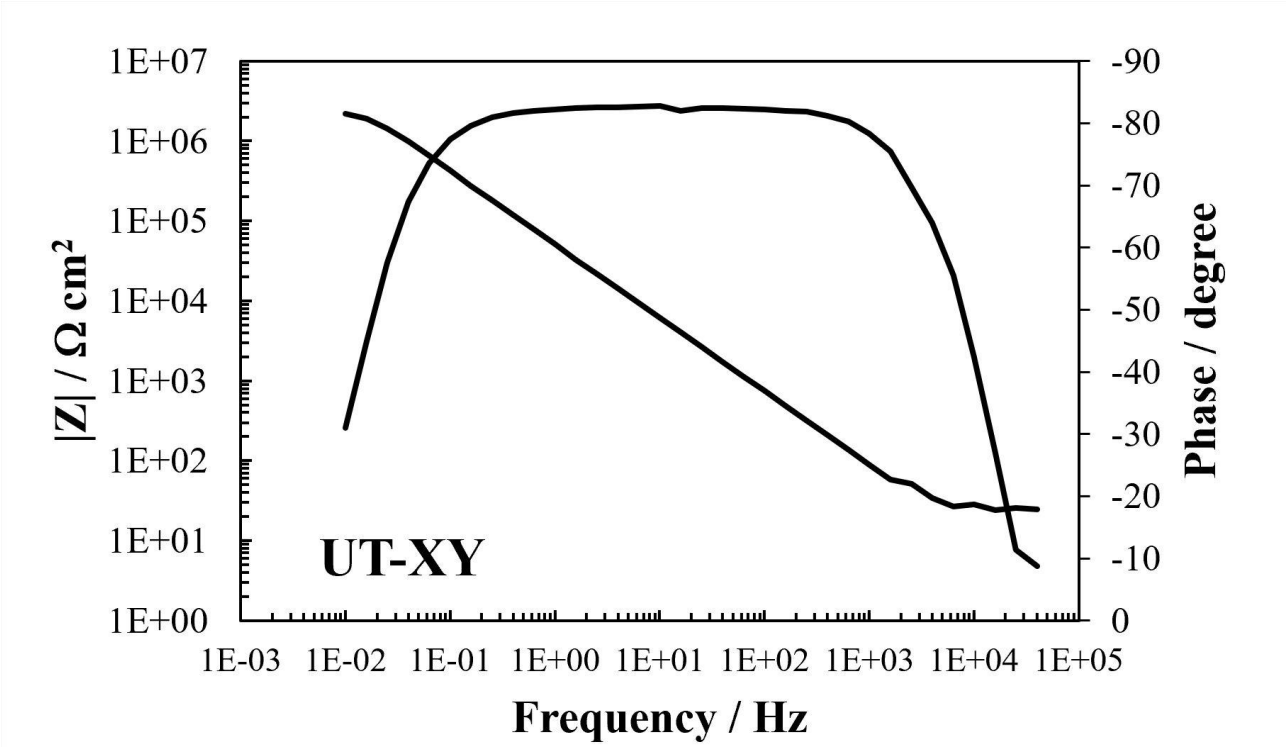

a)

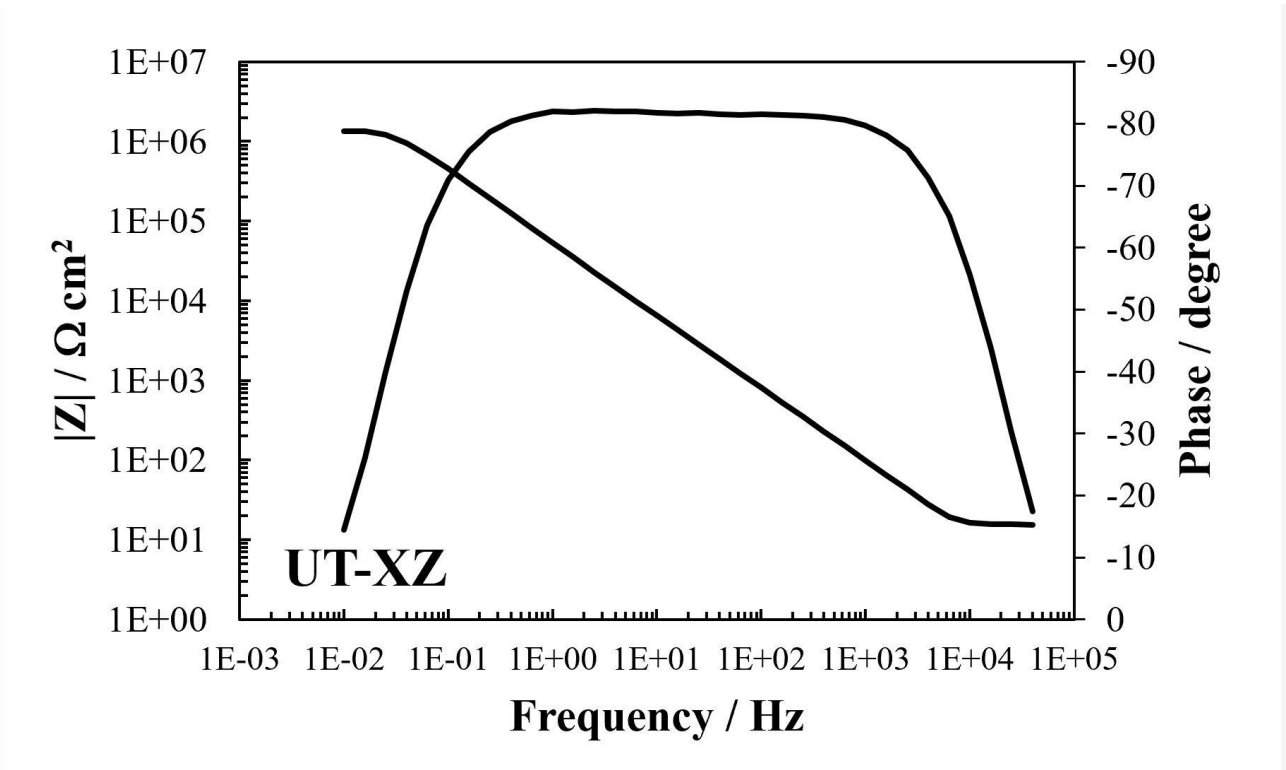

b)

Fig. 2. Example EIS spectrum of the UT specimen immediately after dipping in 0.02 M NaCl solution at 23 °C; a) XY specimen and b) XZ specimen

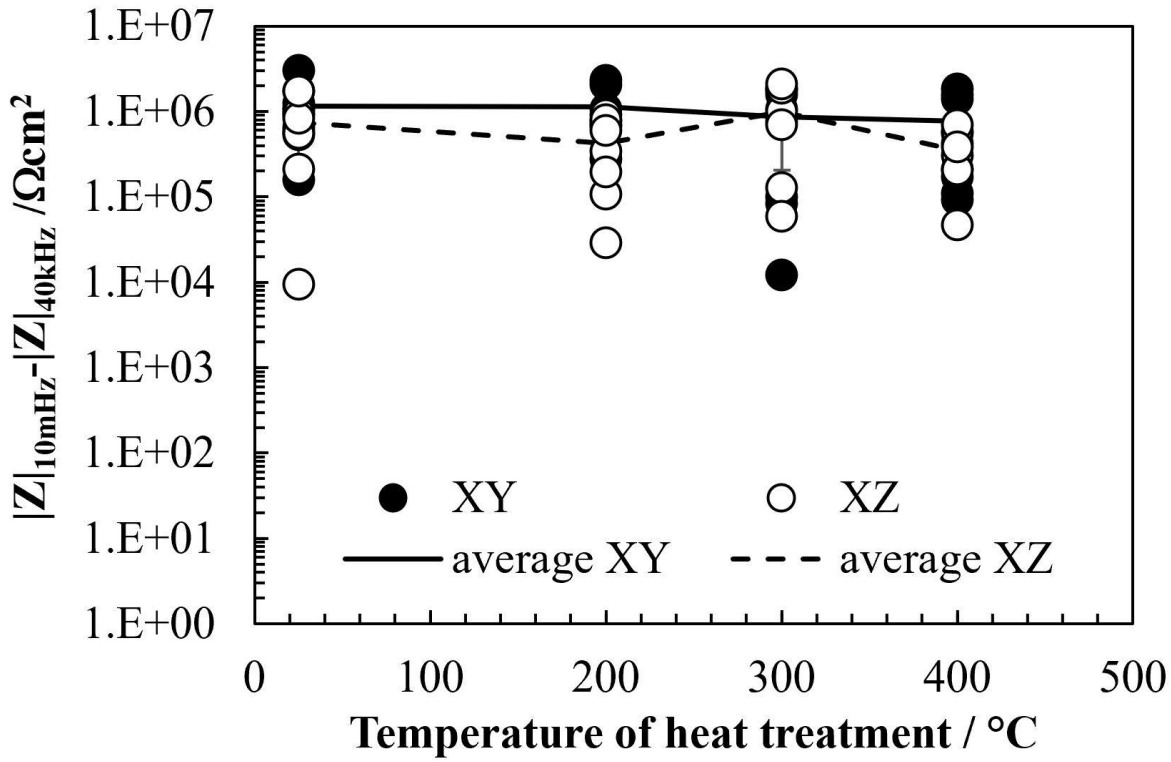

Fig. 3. Effect of heat treatment temperature on the difference in electrochemical impedance modulus at 10 mHz and 40 kHz in 0.02 M NaCl solution at 23 °C

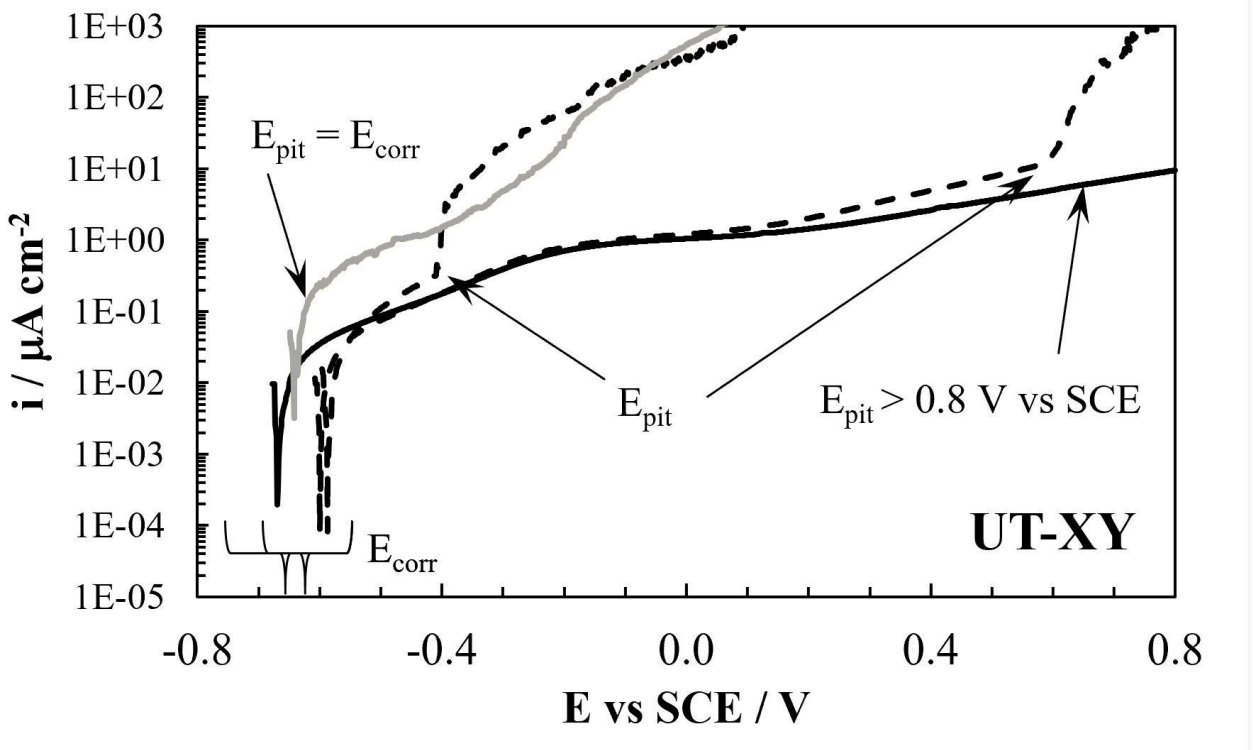

Fig. 4. Potentiodynamic curves of the UT-XY specimens in 0.02 M NaCl solution at 23 °C, showing their different behaviors

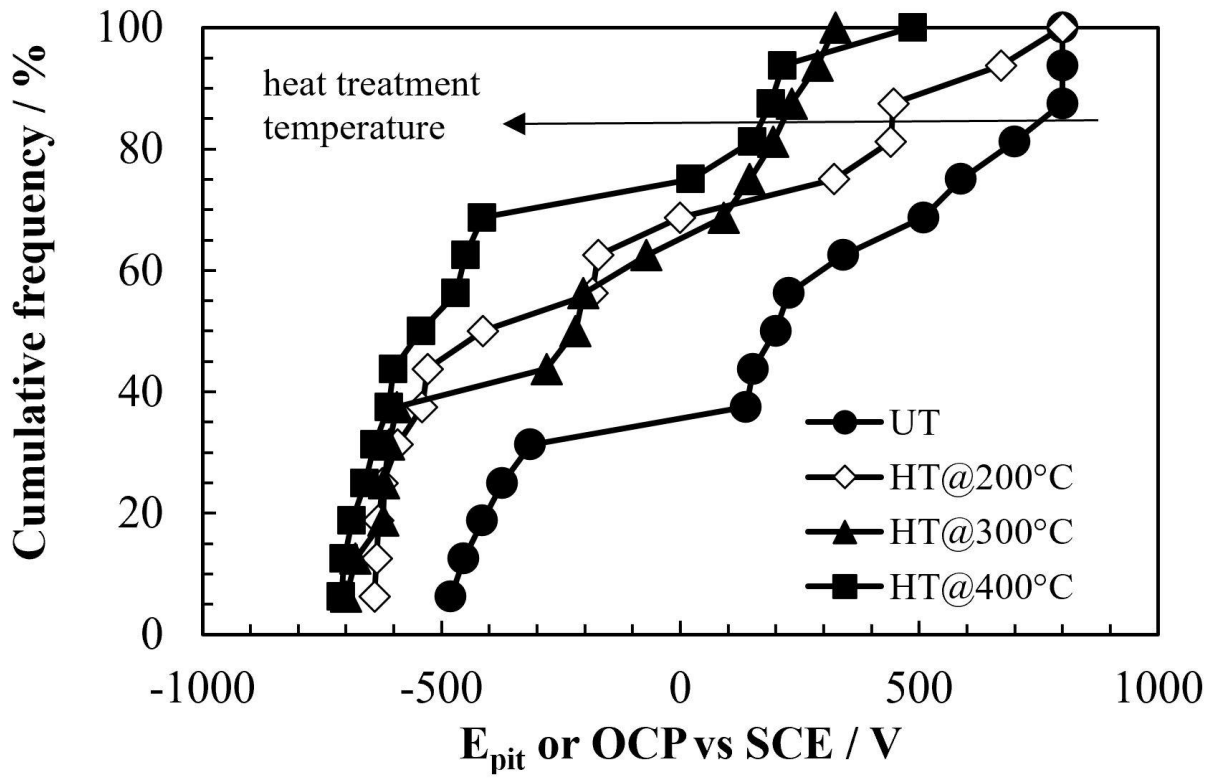

Fig. 5. Effect of heat treatment temperature on the cumulate frequency of the pitting potentials (16 specimens) (or OCP for the pitting was initiated during the equilibration time) in 0.02 M NaCl solution at 23°C (Black dots: UT; White diamonds: HT200°C; Black triangles: HT300°C; Black squares: HT400°C)

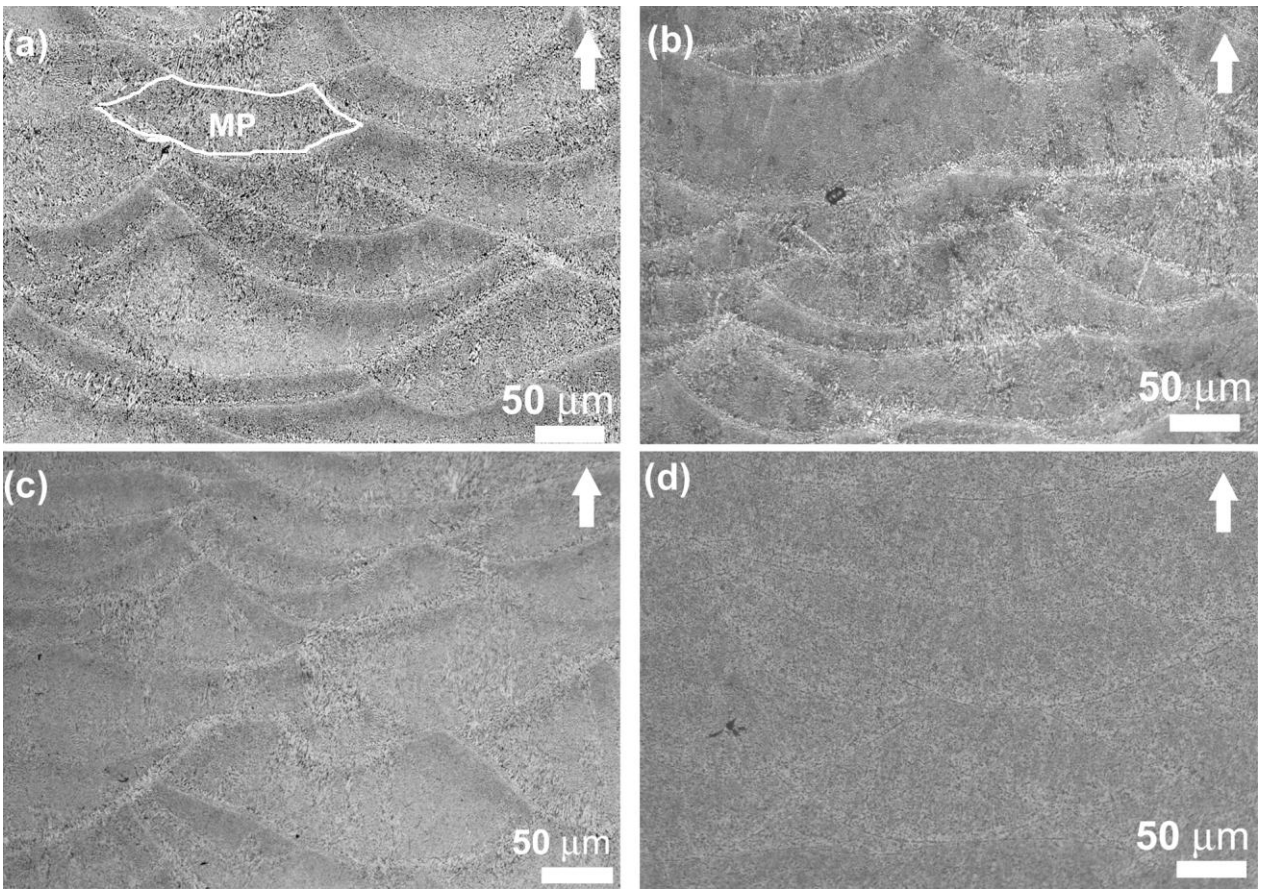

Fig. 6. Microstructure evolution (Keller attack) of AlSi10Mg (XZ plane) using different post-processing treatments: (a) untreated specimen, and specimen heat-treated for 2 h at (b) 200 °C, (c) 300 °C, and (d) 400 °C. The white arrows indicate the building direction (along z-axis)

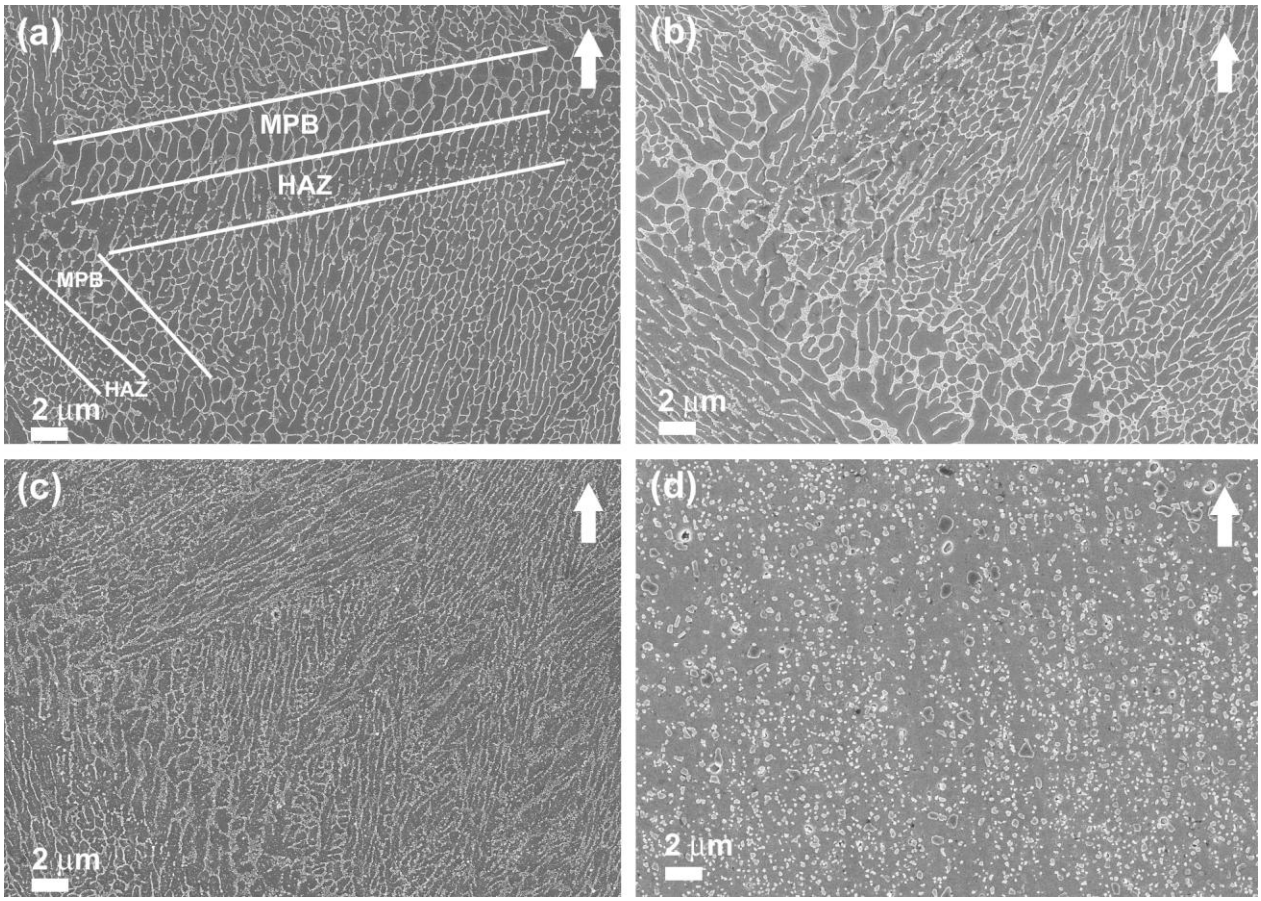

Fig. 7. High-magnification micrographs at the edge of MP of the AlSi10Mg XZ specimens (a) untreated, (b) after stress relieving treatment at 200°C for 2 hours, (c) after stress relieving treatment at 300°C for 2 hours and (d) after stress relieving treatment at 200°C for 2 hours. The white arrows indicate the building direction (along z-axis)

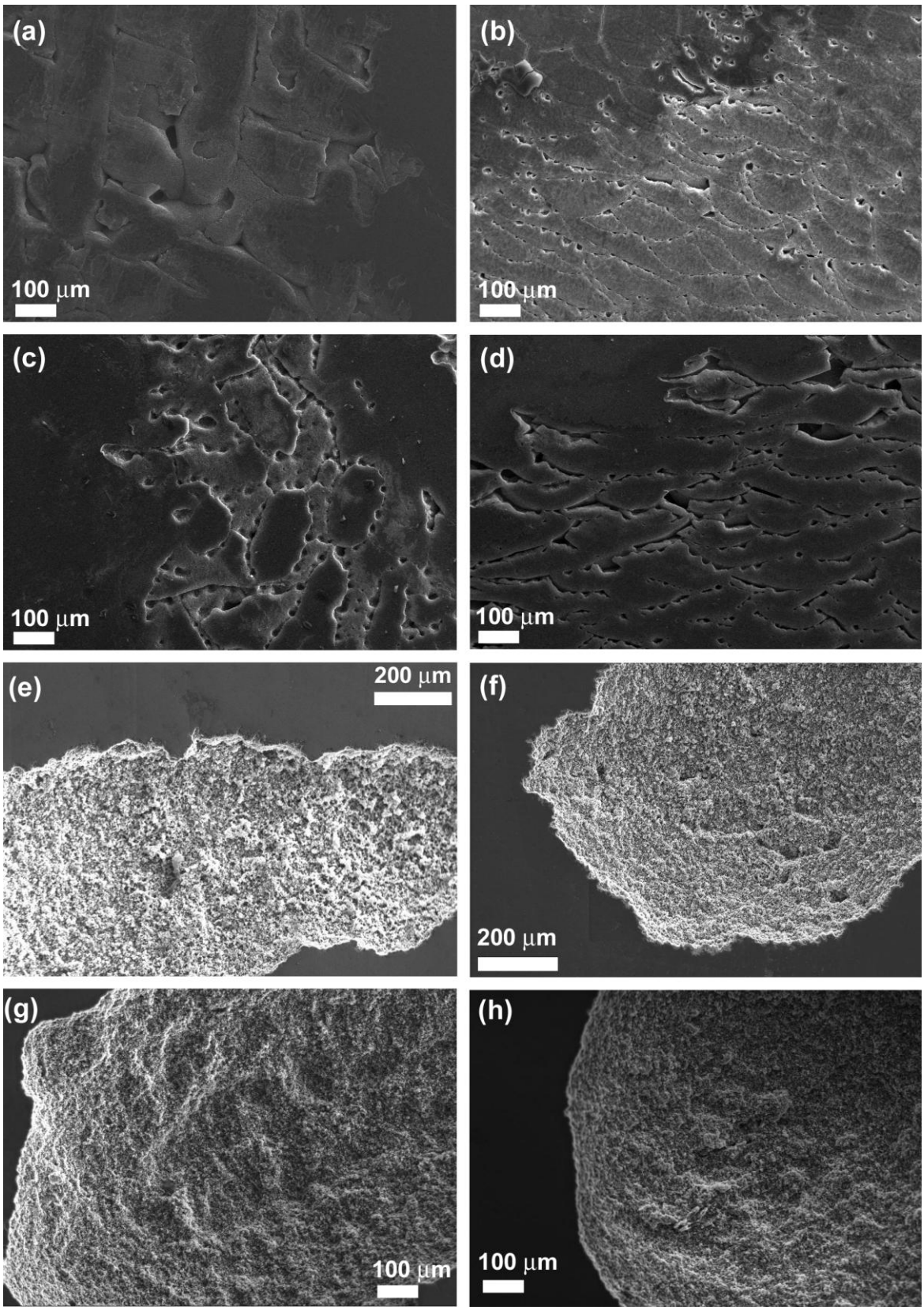

Fig. 8 Morphology of corrosion after the potentiodynamic tests. (a) UT-XY, (b) UT-XZ, (c) HT@200°C-XY, (d) HT@200°C-XZ, (e) HT@300°C-XY, (f) HT@300°C-XZ, (g) HT@400°C-XY, and (h) HT@400°C-XZ

Table 1 Nominal chemical composition of the powder

Table 1: Nominal chemical composition of the powder.

Element	Si	**Fe**	**Cu**	**Mn**	**Mg**	**Ni**	**Zn**	**Ti**	**Al**
% weight	9-11	≤0.55	≤0.05	≤0.45	0.2-0.45	≤0.05	≤0.1	≤0.15	bulk

figure 1 OCP values
Click here to download high resolution image

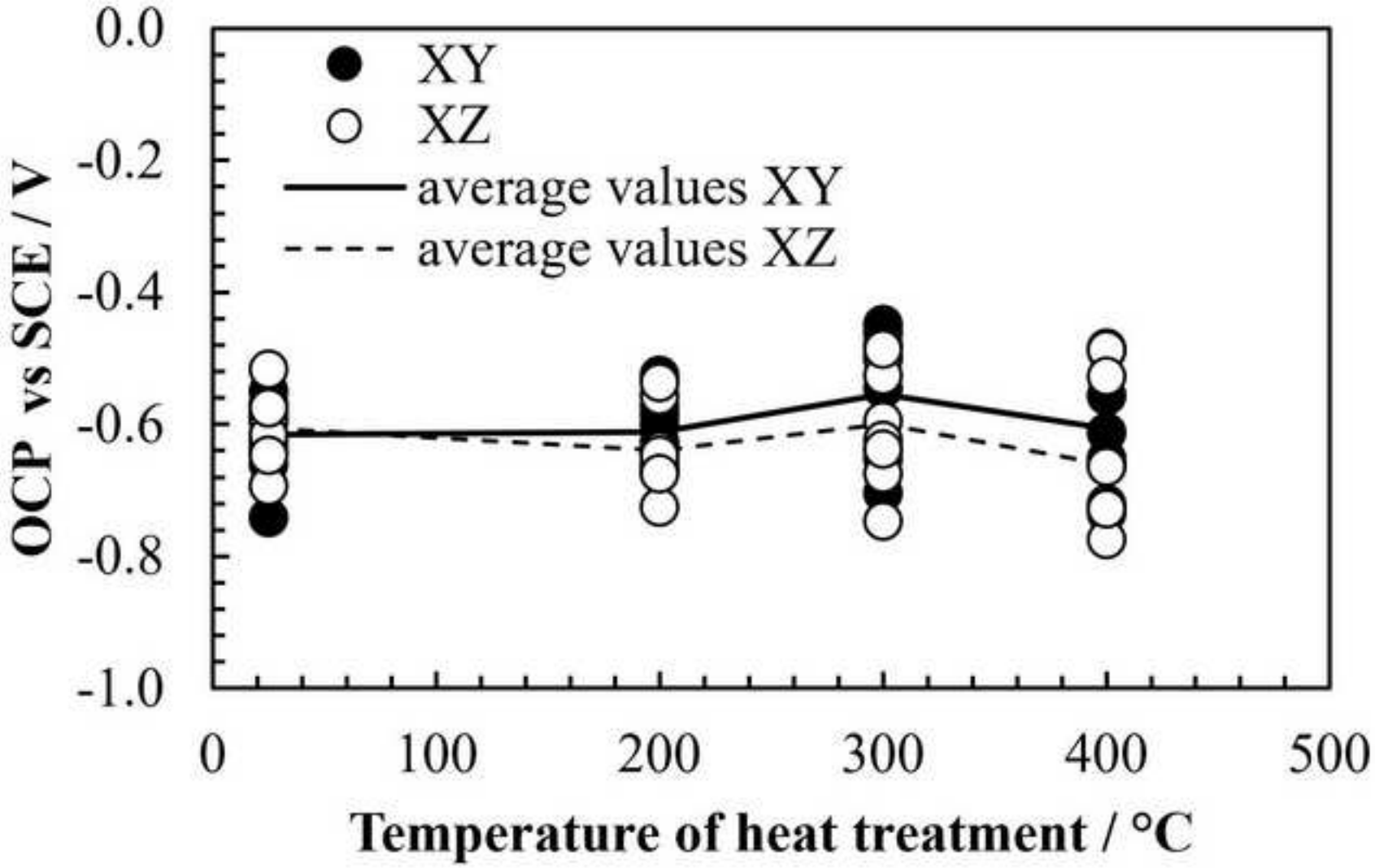

figure 2 a EIS spectrum XY

Click here to download high resolution image

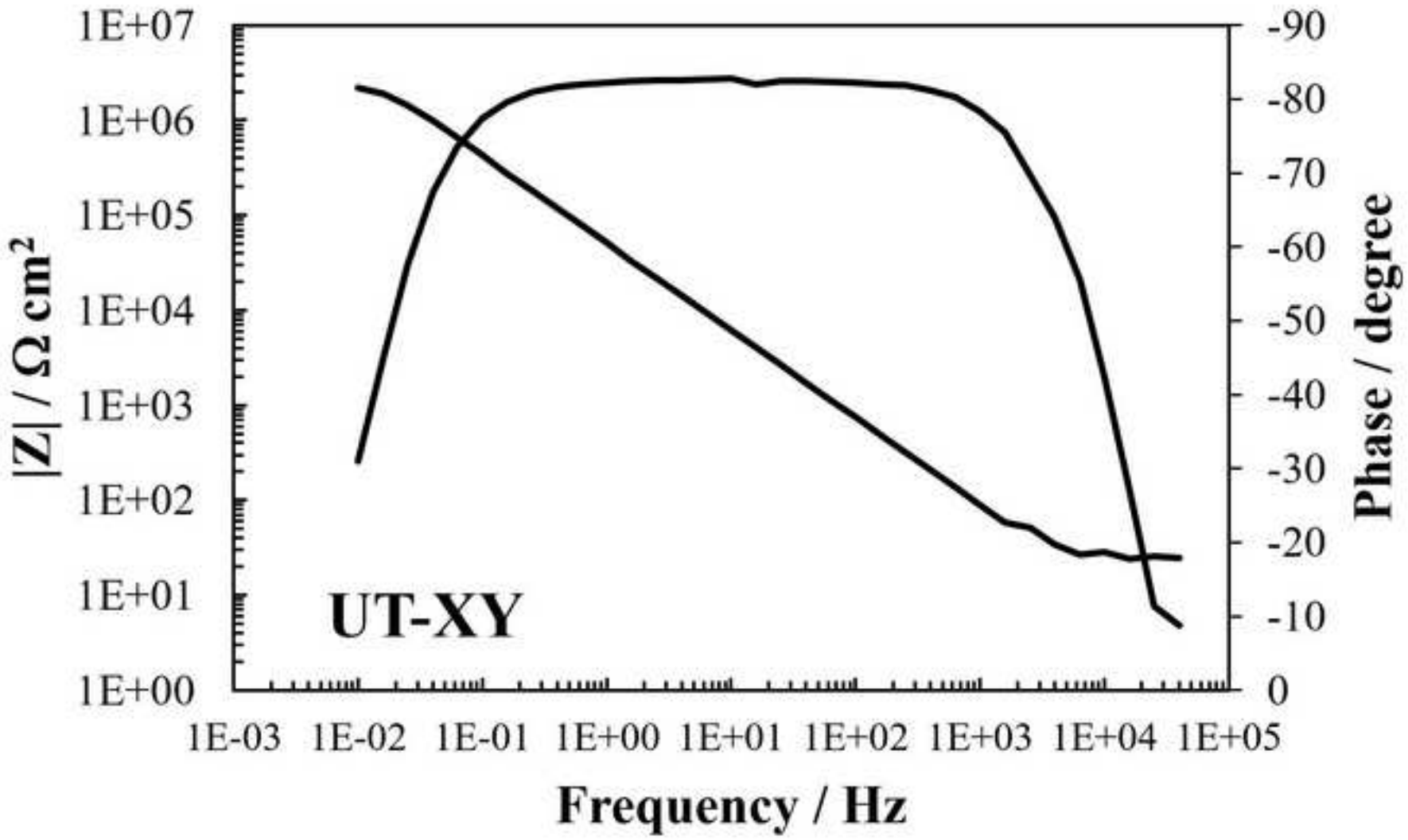

figure 2 b EIS spectrum XZ

Click here to download high resolution image

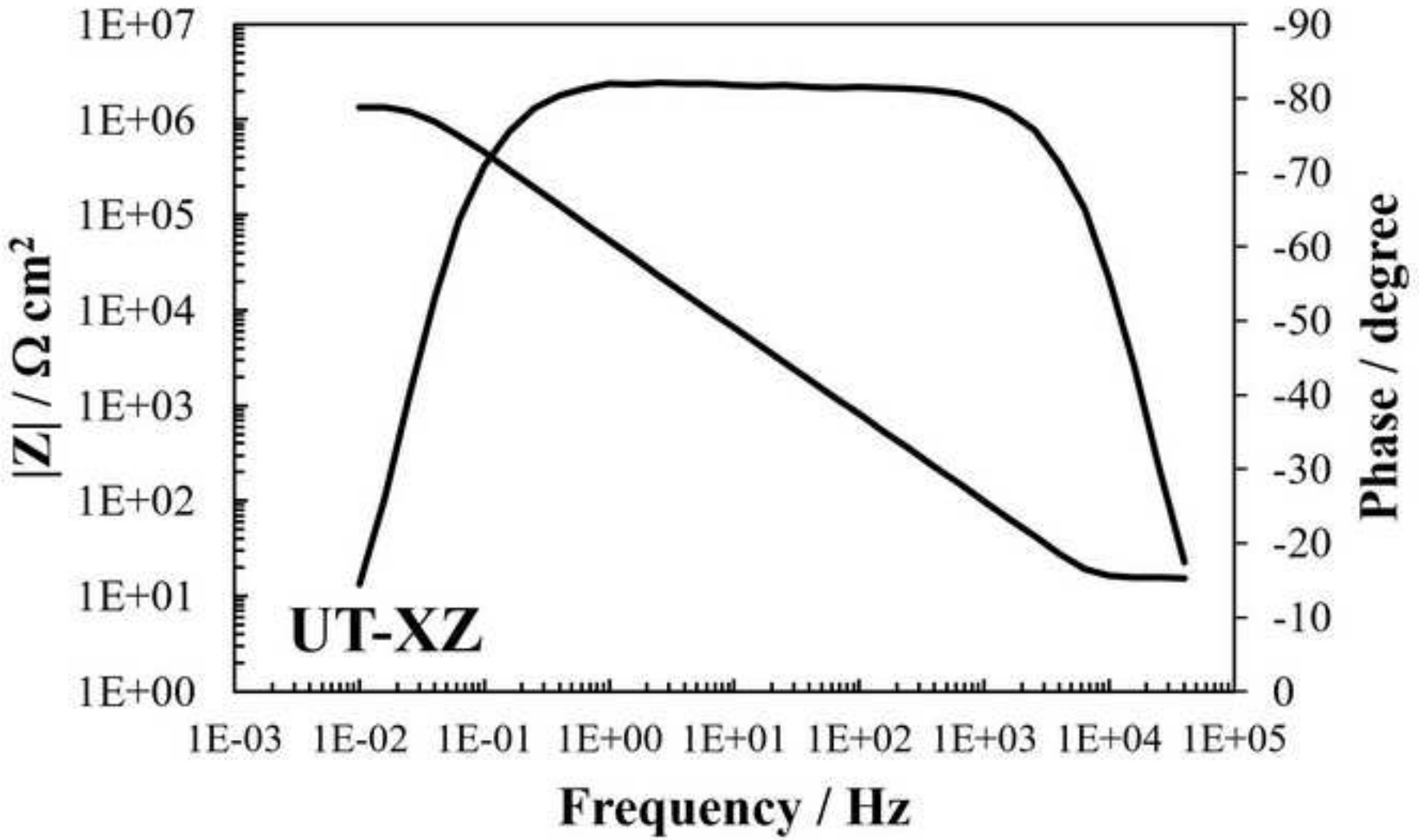

figure 3 Rct

Click here to download high resolution image

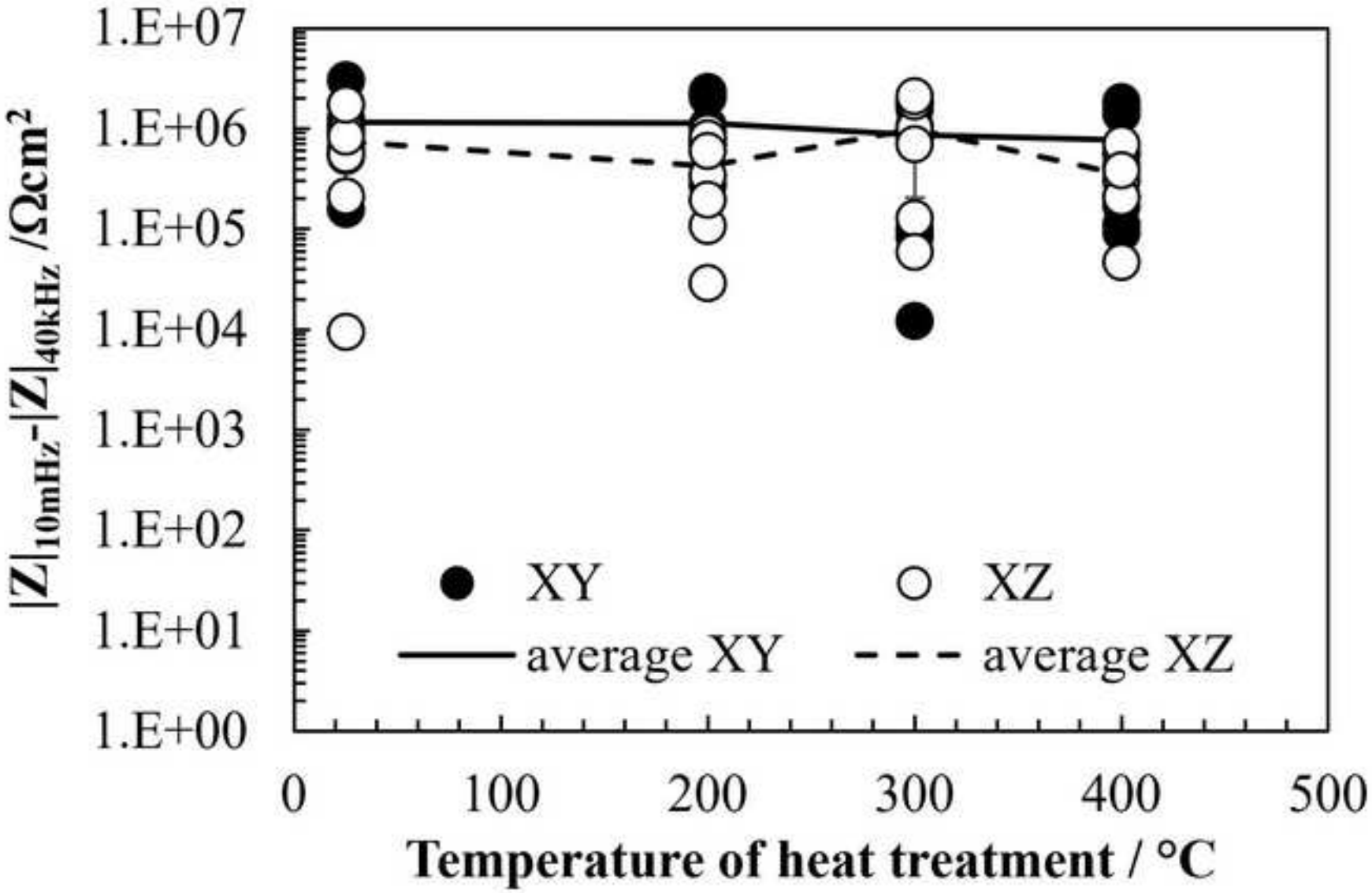

figure 4 potentiodynamic curves
Click here to download high resolution image

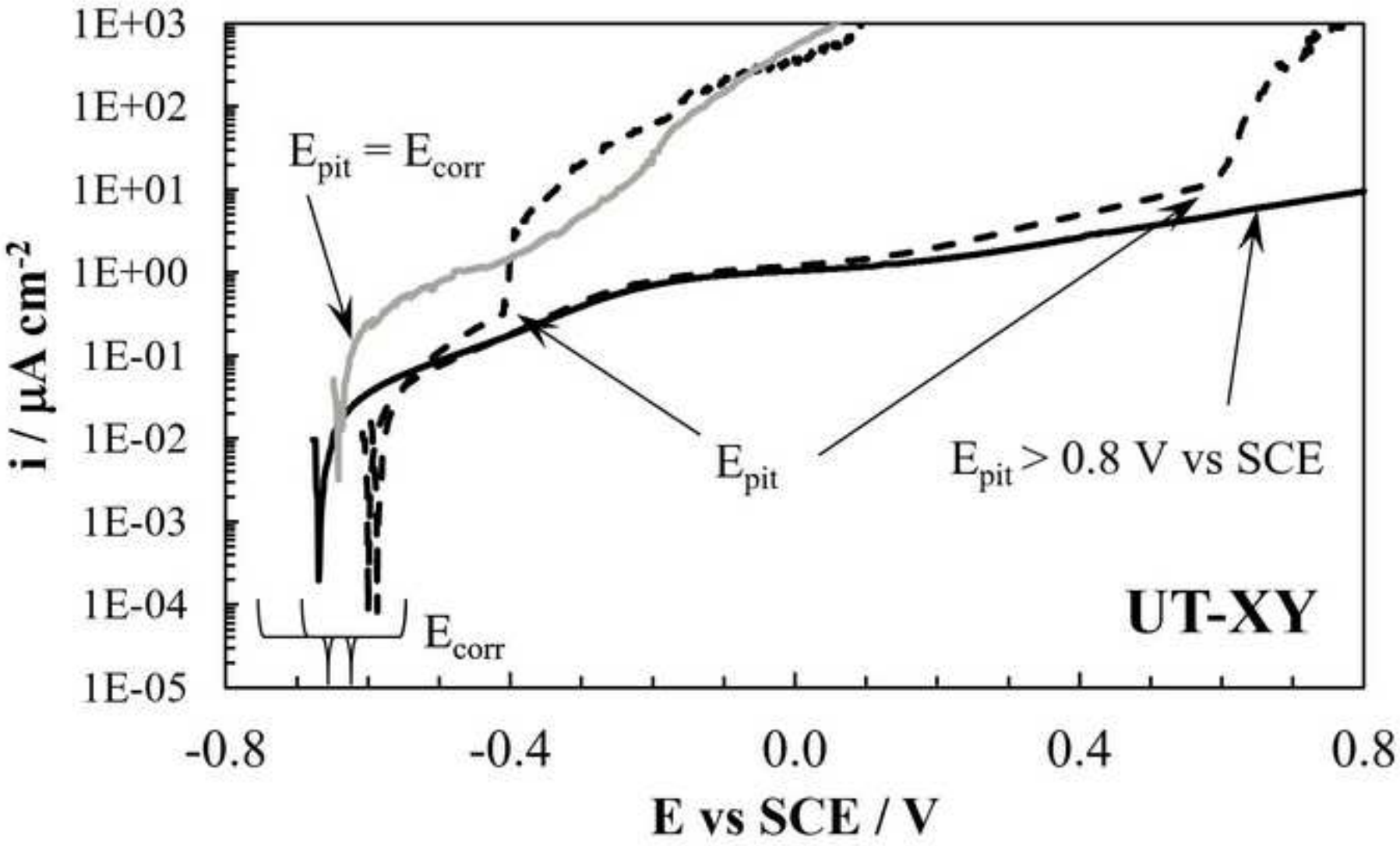

figure 5 frequency distributions pitting potentials
Click here to download high resolution image

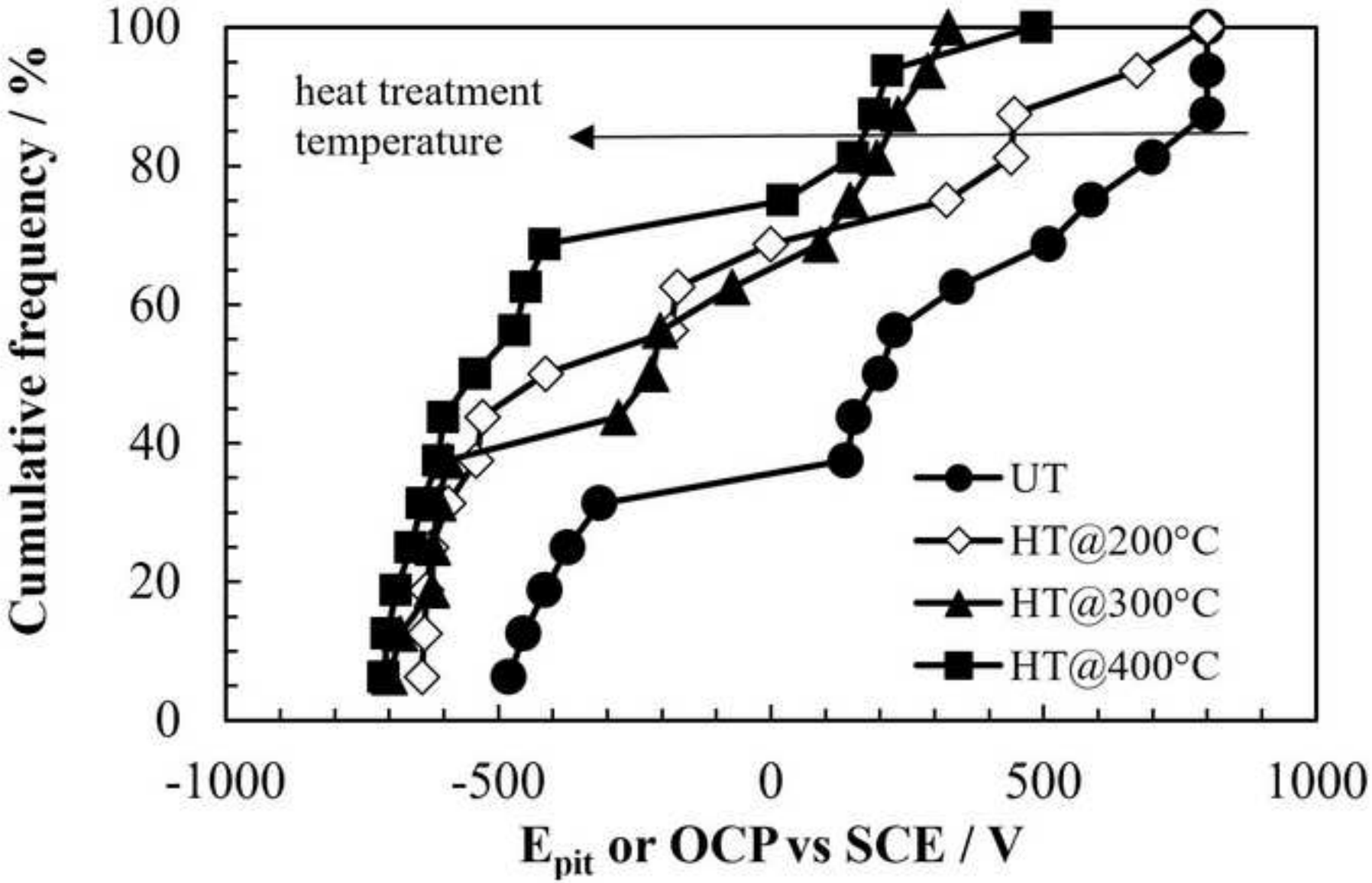

figure 6 microstructure
Click here to download high resolution image

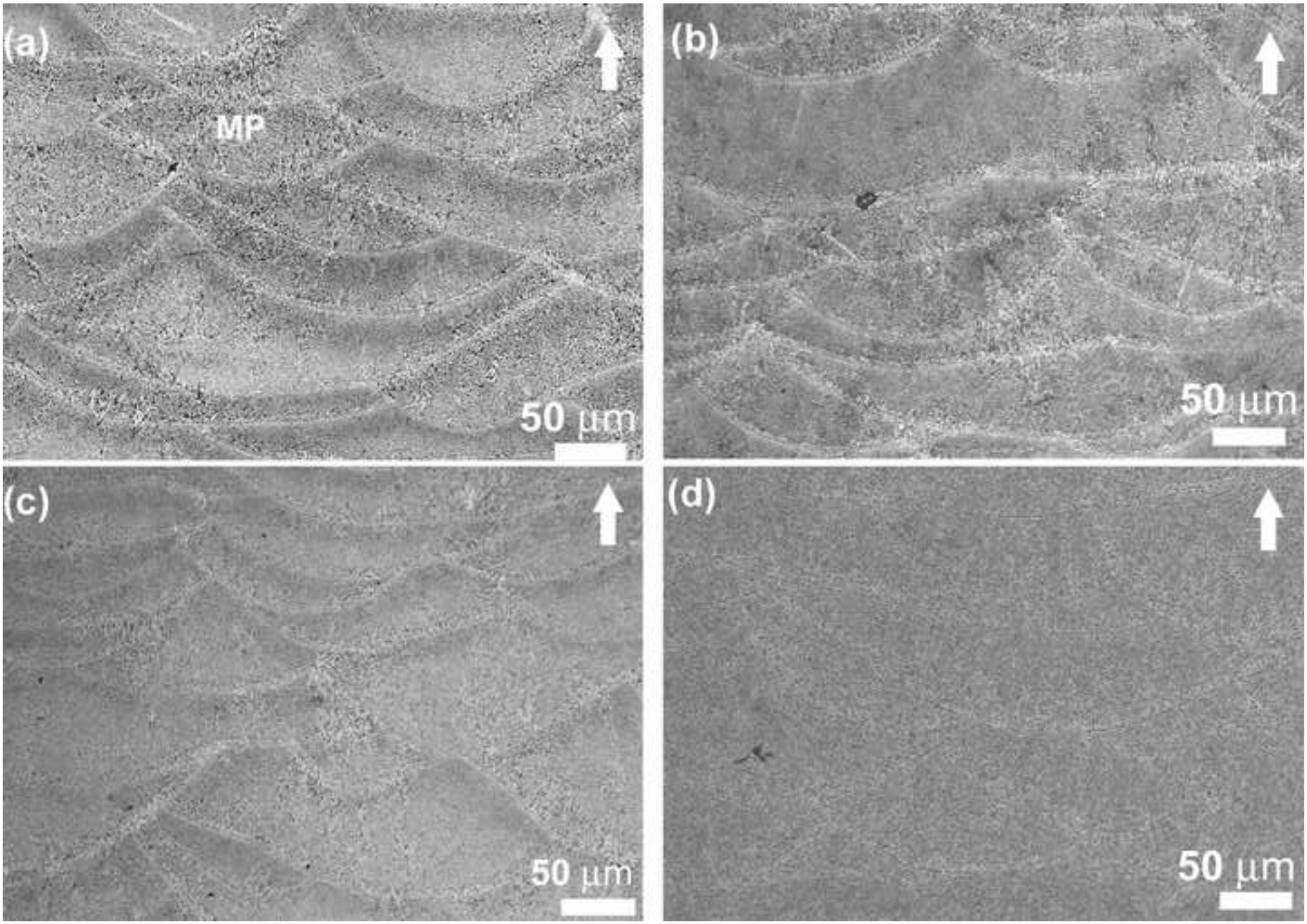

figure 7 SEM microstructure
Click here to download high resolution image

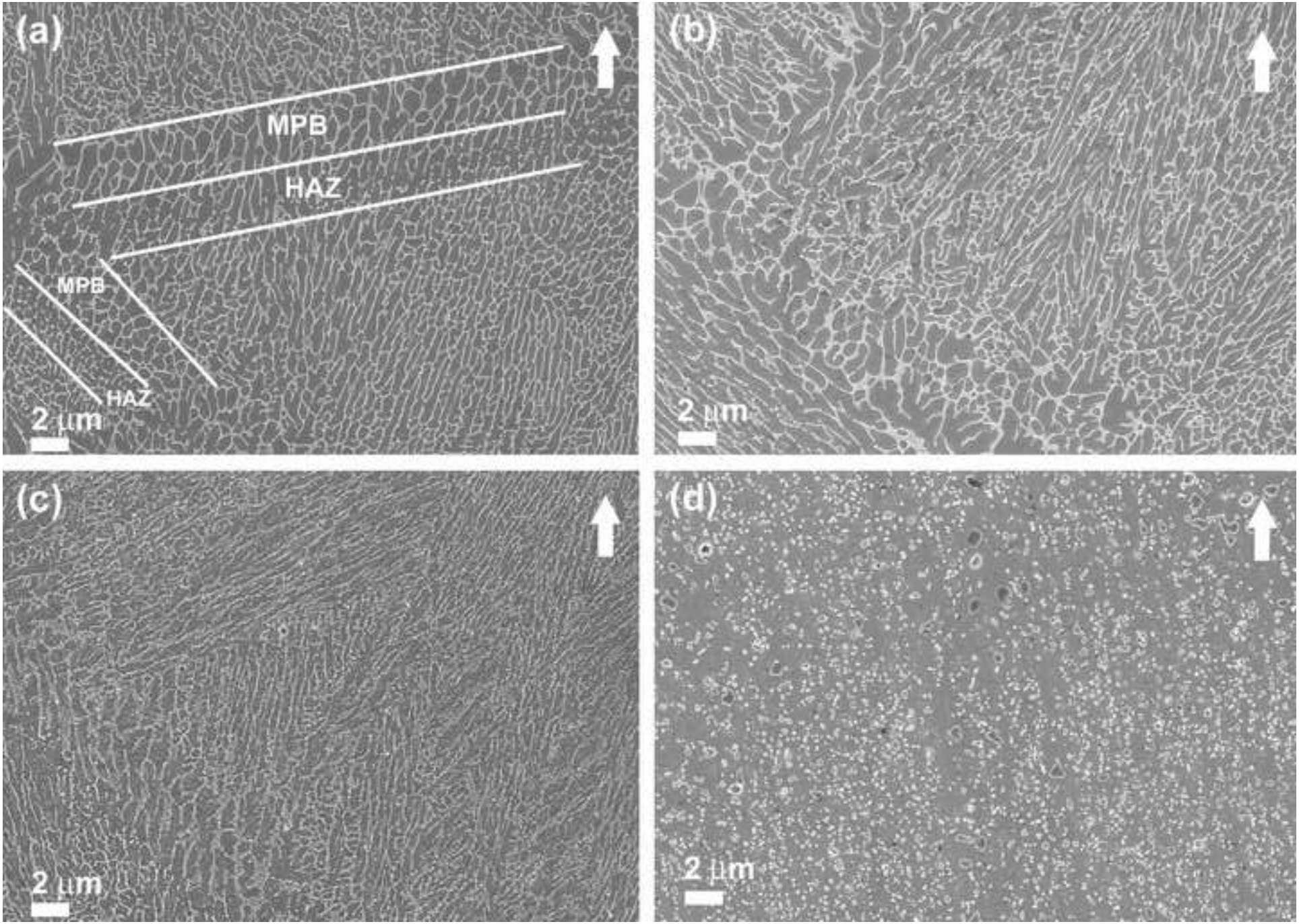

figure 8 morphology of attack
Click here to download high resolution image

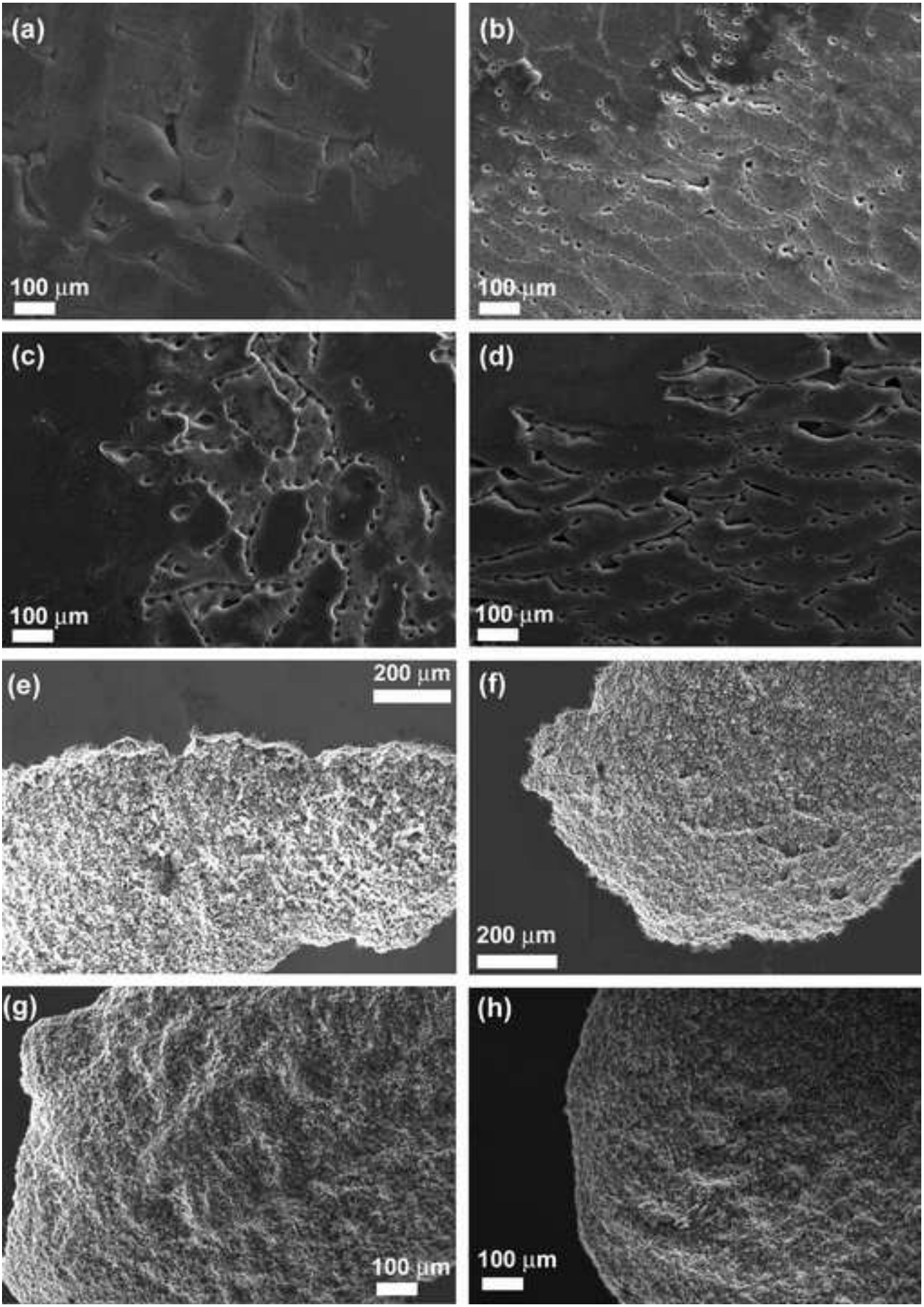

Supplementary Materials

Click here to download Supplementary Materials: Table supplementary.docx